Structure-Dependent Electrocatalytic Properties of Cu 2 O Nanocrystals for Oxygen Reduction Reaction

DATASET *in* THE JOURNAL OF PHYSICAL CHEMISTRY C · JUNE 2013

Impact Factor: 4.77 · DOI: 10.1021/jp403655y

7 AUTHORS, INCLUDING:

Qing Li
Brown University
65 PUBLICATIONS **922** CITATIONS
SEE PROFILE

Ping Xu
Harbin Institute of Technology
102 PUBLICATIONS **2,935** CITATIONS
SEE PROFILE

Shijian Zheng
Los Alamos National Laboratory
42 PUBLICATIONS **588** CITATIONS
SEE PROFILE

THE JOURNAL OF PHYSICAL CHEMISTRY C

Article

pubs.acs.org/JPCC

Structure-Dependent Electrocatalytic Properties of Cu_2O Nanocrystals for Oxygen Reduction Reaction

Qing Li,[†,§] Ping Xu,*[,†,‡] Bin Zhang,[†] Hsinhan Tsai,[‡] Shijian Zheng,[§] Gang Wu,*[,§] and Hsing-Lin Wang*[,‡]

[†]Department of Chemistry, Harbin Institute of Technology, Harbin 150001, China

[‡]Chemistry Division, Los Alamos National Laboratory, Los Alamos, New Mexico 87545, United States

[§]Materials Physics and Applications Division, Los Alamos National Laboratory, Los Alamos, New Mexico 87545, United States

Supporting Information

ABSTRACT: Cu_2O nanocrystals with different morphologies are synthesized via a reductive solution route by controlling the reaction time and using different capping agents. Introducing poly(ethylene glycol) (PEG) leads to nearly monodispersed Cu_2O nanocubes with 40 nm size and dominant {100} crystal planes. With prolonged reaction time, the nanocubes are truncated and transformed into sphere-like nanocrystals with more {111} planes exposed. In the presence of poly(vinyl pyrrolidone) (PVP), porous Cu_2O nanocrystals with both {100} and {111} planes present are produced. The structure-dependent electrocatalytic activity of Cu_2O nanocrystals toward oxygen reduction reaction (ORR) has been studied in alkaline electrolyte. The electrocatalytic activity measured on Cu_2O {100} is higher than that on Cu_2O {111}. In addition, the Cu_2O nanocubes with dominant {100} crystal planes show the highest four-electron selectivity (n = 3.7) and lowest peroxide yield (15%) during the ORR. Kinetics analysis indicates that the ORR mechanism on Cu_2O nanocrystals is controlled simultaneously by charge transfer and intermediate migration. The Cu_2O nanocrystals also show better methanol tolerance and durability for ORR than the commercial Pt/C materials.

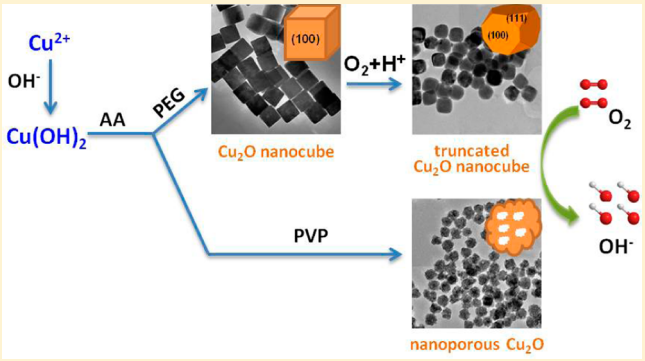

I. INTRODUCTION

Catalytic properties of nanocrystals can be easily tailored by tuning either their composition (electronic structure) or morphology (surface atomic arrangement and coordination).[1] It has been demonstrated that different crystal faces of Pt or Pt−Pd nanocrystals exhibit a significant difference in catalytic properties for electro-oxidation and electro-reduction reactions.[1,2] Oxygen reduction reaction (ORR) has become one of the most important electrochemical reactions crucial to a variety of electrochemical energy storage and conversion technologies such as fuel cell and metal-air batteries.[3,4] Although Pt is most effective to catalyze hydrogen oxidation and oxygen reduction in fuel cells,[5,6] high cost, poor tolerance to fuel crossover and easy CO poisoning have greatly limited its use toward commercial applications. Thus, highly efficient, cost-effective nonprecious-metal catalysts (NPMCs) are considered a holey grail in developing next generation catalysts for energy device applications.[4,7] NPMCs synthesized from earth-abundant elements have the potential to efficiently catalyze the ORR, generating clean energy via a direct electrochemical conversion. Some promising NPMCs have been studied in the past decade, including organometallic components, nonprecious-metal chalcogenides, and nitrogen-doped carbon catalysts.[7,8] Transition metal oxides, sulfides, carbides or nitrides such as Co_3O_4,[9] MnO_2,[10] TiO_2,[11] NbO_2,[12] Ta_2O_5,[13] Co_9S_8,[14] WC,[15] and TiN[16] have also been found to be catalytically active for ORR, indicating that versatile NPMCs might be ideal candidates substituting noble metal catalysts.

Cuprous oxide (Cu_2O), with a high optical absorption coefficient and a bulk band gap of 2.2 eV, has been recognized as an excellent candidate for applications in low-cost photovoltaics,[17,18] high-efficiency photocatalysis,[19−22] sensitive surface enhanced Raman spectroscopy platform,[23] and even high-performance electrode materials.[24,25] Recently, Cu_2O nanocrystals of various geometries have been synthesized through bottom-up approaches, including nanowires,[26] nanocubes,[27−30] polyhedra,[31−35] and hollow or porous spherical structures.[36−40] Recently, Guo and his co-workers found that Cu_2O nanoparticles dispersed on reduced graphene oxide (RGO) can be used as an efficient electrocatalyst for ORR,[41] which indicates that Cu_2O may hold great promise to be used as one of the NPMCs. However, morphology- and/or structure-dependent optical and catalytic properties of Cu_2O nanocrystals have not been fully realized. A greater understanding of the electrocatalytic properties of Cu_2O nanocrystals as a function of crystal structures may provide valuable insights and principles for rational design of metal oxide catalyst in clean energy applications.

Received: April 13, 2013
Revised: May 30, 2013
Published: June 18, 2013

In this work, Cu_2O nanocrystals with different morphologies and structures have been prepared via a reductive solution chemistry route by applying different capping agents during the synthesis. As-prepared Cu_2O nanocrystals with different morphologies are actually dominated by specific crystal faces, allowing us to study the structure-dependent electrocatalytic activity of Cu_2O nanocrystals for the ORR.

II. EXPERIMENTAL SECTION

Materials. Copper acetate monohydrate ($Cu(Ac)_2{\cdot}H_2O$, ACS reagent, Acros), sodium hydroxide (≥98%, Aldrich), ascorbic acid (AA, 99%, Acros), poly(ethylene glycol) (PEG, mw = 10 000, Aldrich), and poly(vinyl pyrrolidone) (PVP, mw = 40 000, Aldrich) are used as received.

Synthesis of Cu_2O Nanocrystals. Cu_2O nanocrystals were prepared through a modified reductive solution chemistry route.[30] In a typical procedure, 0.5 g of PEG was first dissolved in 10 mL of $Cu(Ac)_2$ aqueous solution (0.1 mM). Once PEG was completely dissolved, 50 μL of NaOH solution (6.0 M) was dropwise added. Upon addition, the solution immediately changed to blue color, indicating the formation of $Cu(OH)_2$ nanoparticles. After 10 min, 0.2 mL of AA solution (1 M) was dropwise added to the solution and it slowly turned to orange color. We call this procedure "PEG-assisted synthesis of Cu_2O nanocrystals". The products (nanoparticles) are collected at different reaction time periods. In the case of the PVP-assisted synthesis, all of experimental procedures were identical to the PEG-assisted route, except that 0.50 g of PEG was replaced by 0.56 g of PVP. The obtained Cu_2O nanocrystals were rinsed with deionized water for at least five times, and then with ethanol for three times to remove the polymer residuals, after which the Cu_2O samples were dried under vacuum.

Characterization. Transmission electron microscopic (TEM) images of the Cu_2O nanocrystals were taken on a JEOL-3000F electron microscope. TEM samples were prepared by dropping the nanocrystal solution onto a carbon coated copper grid. Scanning electron microscopic (SEM) images were taken on a FEI Inspect electron microscope. UV−vis spectra were measured on a Varian Cary 500 Scan UV−vis−NIR spectrophotometer in the range between 400−900 nm. The X-ray diffraction (XRD) patterns of the samples were conducted on a Rigaku/Max-3A X-ray diffractometer with Cu Kα radiation (λ = 1.54178 Å), the operation voltage and current maintained at 40 kV and 40 mA, respectively.

Electrocatalysis. In order to determine the electrocatalytic activity and four-electron selectivity of ORR on Cu_2O catalysts, rotating ring and disk electrodes (RRDE) were employed in a conventional three-electrode cell with 0.1 M KOH solution at room temperature. A graphite rod and an Ag/AgCl (3.0 M NaCl) electrode were used as the counter and reference electrodes, respectively. CHI Electrochemical Station (model 750b) was used for all electroanalytical experiments. All potentials have been converted relative to the reversible hydrogen electrode (RHE) scale. In order to prepare catalyst ink, each Cu_2O sample was ultrasonically dispersed in an alcoholic solution containing 5 wt % Nafion ionomer for 1 h. The ink was then applied to the glassy-carbon disk of RRDE with a geometric area of 0.245 cm^2. The Cu_2O and commercial Pt/C (20%) catalysts loading were controlled at 0.6 mg cm^{-2} and 20 μg cm^{-2}, respectively. As the conductivity of Cu_2O itself may be insufficient, in addition to directly testing the ORR activity on Cu_2O nanocrystal samples, carbon-dispersed Cu_2O samples were prepared specially for the RRDE tests. The commercially available Ketjen Black EC 300J material was adopted as the carbon support in this work, because of its high BET surface area (about 950 m^2/g), large fraction of mesophase and corrosion resistance. In doing so, 10 mg of Ketjenblack was mixed with 10 mg of Cu_2O samples in 2 mL of isopropanol solution with continuously stirring for 24 h before testing Steady-state polarization plots of ORR were recorded in an O_2-saturated electrolyte from 0.97 to 0.30 V. The potential was held for 30 s at each point with a step of 0.03 V so as to eliminate the possible capacitance current. The four-electron selectivity during the ORR was determined by setting the ring potential at 1.1 V to oxidize the two-electron product, peroxide. According to eq 1 and 2, the peroxide yield and the electron transfer number (n) can be calculated, respectively.[42]

$$\text{peroxide yield}(\%) = 200 \times \frac{I_R/N}{(I_R/N) + I_D} \quad (1)$$

$$n = 4 \times \frac{I_D}{(I_R/N) + I_D} \quad (2)$$

where I_D and I_R are the disk and ring currents, respectively, and N is the ring collection efficiency that was calibrated to be 36%.

III. RESULTS AND DISCUSSION

Traditional syntheses of Cu_2O through chemical and electrochemical routes commonly leads to micrometer sized particles,[43,44] which have a limited surface area and thus constrain their applications in optical and energy devices. Here, Cu_2O nanocrystals with sizes less than 50 nm can be prepared via a modified reductive pathway. First, Cu^{2+} ions are precipitated into $Cu(OH)_2$ nanoparticles in blue color (eq 3). Next, they are reduced by ascorbic acid (AA) to form Cu_2O nanocrystals (eq 4), where AA* means the oxidized form of AA. X-ray diffraction (XRD) measurements have confirmed that the as-prepared samples are pure Cu_2O nanocrystals, without any other copper impurities (Figure S1). It is important to note that, during the preparation of Cu_2O nanocrystals, the solution color changes from orange, brown, light-brown, to almost colorless as the reaction proceeds, indicating the possible oxidation of the Cu_2O nanocrystals to Cu^{2+} as shown in eq 3. One control experiment to confirm our hypothesis is to purge the reaction system with N_2 to remove oxygen from water, which has led to a much slower change in solution color, suggesting a reduced oxidation rate when most of the oxygen is eliminated in the solution. The use of extremely low Cu^{2+} ions concentration of (0.1 mM) is also crucial for producing Cu_2O nanocrystals as higher concentrations typically lead to submicrometer or micrometer sized particles (Figure S2). Moreover, different capping agents used for size control can lead to dramatic morphological change for the Cu_2O nanocrystals. As can be seen in Figure 1a, the TEM and SEM images reveal monodispersed Cu_2O nanocubes with a size of 40 nm at a reaction time of 30 min when PEG is used. The HR-TEM image in Figure 1b shows that these crystalline nanocubes mainly have their {100} crystal planes exposed, and the selected area electron diffraction (SAED), inset of Figure 1b, confirms that these nanocubes are perfect single crystals. At a prolonged reaction time of 2 h, solution color becomes lighter, and sphere-like Cu_2O nanocrystals with a smaller size (~35 nm) are formed (Figure 1c), presumably due to truncation of the nanocube around the corners through oxidation by oxygen and proton ions, as suggested in eq 5.

dx.doi.org/10.1021/jp403655y | J. Phys. Chem. C 2013, 117, 13872−13878

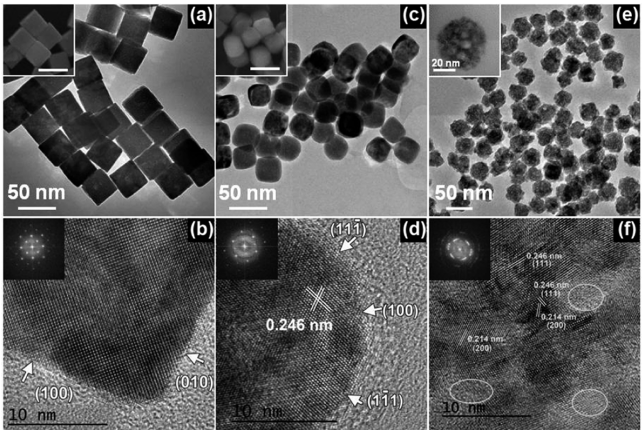

Figure 1. TEM and HR-TEM images of the PEG-assisted Cu_2O nanocrystals at a reaction time of 30 min (a and b) and 2 h (c and d), and PVP-assisted Cu_2O nanocrystals at a reaction time of 30 min (e and f). Insets in panels a and c are the SEM images of the corresponding samples, scale bar: 50 nm. Inset in panel e shows a magnified TEM image of the porous structure.

SEM image in Figure 1c also confirms that the nanocubes are truncated into sphere-like crystals with the prolongation of reaction time. A close look at the HR-TEM image (Figure 1d) clearly shows that the corners of these nanocubes are truncated, allowing the exposure of {111} crystal planes. The above results suggest that PEG, as a capping agent, is not enough to prevent {100} facets from being oxidized during the synthesis. Although Cu_2O synthesis has been widely studied and solution color change during the synthesis procedure has been observed,[34] the morphology and structure changes through a truncation process is reported in this work for the first time.

$$Cu^{2+} + 2OH^- \rightarrow Cu(OH)_2 \quad (3)$$

$$Cu(OH)_2 + AA \rightarrow Cu_2O + AA^* \quad (4)$$

$$2Cu_2O + O_2 + 8H^+ \rightarrow 4Cu^{2+} + 4H_2O \quad (5)$$

It is particularly interesting to find that, when PVP is used as the capping agent following the same procedures in making Cu_2O nanocubes, PVP-assisted synthesis leads to formation of porous Cu_2O nanoparticles with sizes of about 40−50 nm (Figure 1e). The HR-TEM image and SAED in Figure 1f reveal both {111} and {100} crystal planes in these nanoporous Cu_2O. In addition, we also observe void spaces (white circles in Figure 1f) in these highly crystallized porous Cu_2O nanoparticles. Note that the change of solution color is much slower in this PVP-assisted procedure, probably due to a better protection from PVP layer on the nanoporous Cu_2O, preventing further oxidation by O_2. Also, no obvious change in either morphology or crystal structure has been found from the PVP-assisted Cu_2O nanoparticles as a function of reaction time, up to 2 h (Figure S3). Though the formation mechanism of porous structures by PVP remains unclear, it has been witnessed in preparing submicrometer Cu_2O particles, and the porous part may have resulted from the etching of the amorphous region inside the Cu_2O crystals.[36] The above results suggest a capping agent effect on the morphology and structure of Cu_2O nanoparticles. However, prolonged reaction time (12 h) will eventually turn the solution color into colorless in both PEG-assisted and PVP-assisted reaction systems, indicating the complete oxidation of Cu_2O nanocrystals to Cu^{2+}, which redissolve back into the solution via the reaction shown in eq 5.

As the optical properties of Cu_2O nanocrystals are well correlated with their morphologies and structures,[36] the optical properties of the three Cu_2O nanoparticles are characterized (Figure 2). The 40 nm Cu_2O nanocubes display an extinction

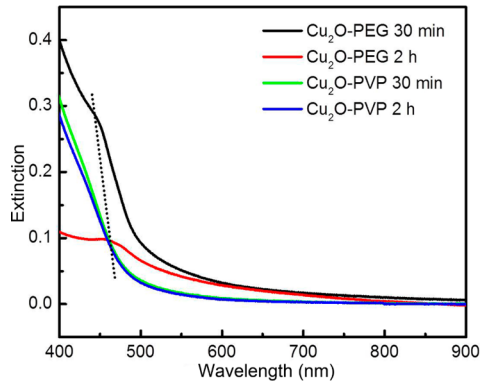

Figure 2. UV−vis spectra of the PEG-assisted and PVP-assisted Cu_2O nanocrystals at a reaction time of 30 min and 2 h.

band at about 445 nm, corresponding to the orange color of the sample collected at 30 min. The absorption becomes much weaker for the truncated sphere-like Cu_2O nanocubes as the solution turns light-brown at a reaction time of 2 h and the absorption peak red-shifts to 463 nm. Our study show clear contrast with results reported by Li et al., who have shown synthesis of 200 nm Cu_2O nanoparticles with an absorption peak at 520 nm.[45] As the size of truncated nanocubes is smaller than that of the nanocubes, the absorption difference should be mainly due to morphology changes. On the other hand, the nanoporous Cu_2O prepared in the presence of PVP show a prominent extinction edge at ~485 nm, and no difference was found for the absorption spectra between samples collected at 30 min and 2 h. The nearly identical absorption spectra for nanoporous Cu_2O collected at different time periods further validates our hypothesis that PVP may better protect nanoporous Cu_2O from reacting with O_2. The absorption of nanoscaled particles typically locates at lower wavelengths than micrometer sized Cu_2O samples (>500 nm).[36,45] In view of the above results, it is interesting to see that the optical properties of Cu_2O show strong correlations with their size, morphology, and especially the crystal structure.

Although size- or morphology-dependent optical properties of Cu_2O particles have been studied,[36] the associated electrocatalytic properties have yet to be determined. Very recently, reduced graphene oxide (RGO)-supported Cu_2O has been used for catalyzing ORR in alkaline solution.[41] However, as graphene-based carbon materials are also good catalysts for ORR in alkaline solution, the exact role of Cu_2O in electrocatalysis has not been clearly elucidated. Thus, it is of great importance to study the structure-dependent catalytic properties of Cu_2O nanoparticles, particularly for ORR. Cyclic voltammograms in N_2-saturated 0.1 M KOH solution indicate that a pair of redox peaks in all three Cu_2O samples, corresponding to the CuO/Cu_2O redox couple (Figure S4).[46] Generally, the current density of CV between 0.2 and 0.5 V is attributed to capacitive current that depends on the electrochemically accessible area, S_a (m^2/g), i.e., the area where the electrolyte enters the internal pore structure. Thus, S_a of Cu_2O

dx.doi.org/10.1021/jp403655y | J. Phys. Chem. C 2013, 117, 13872−13878

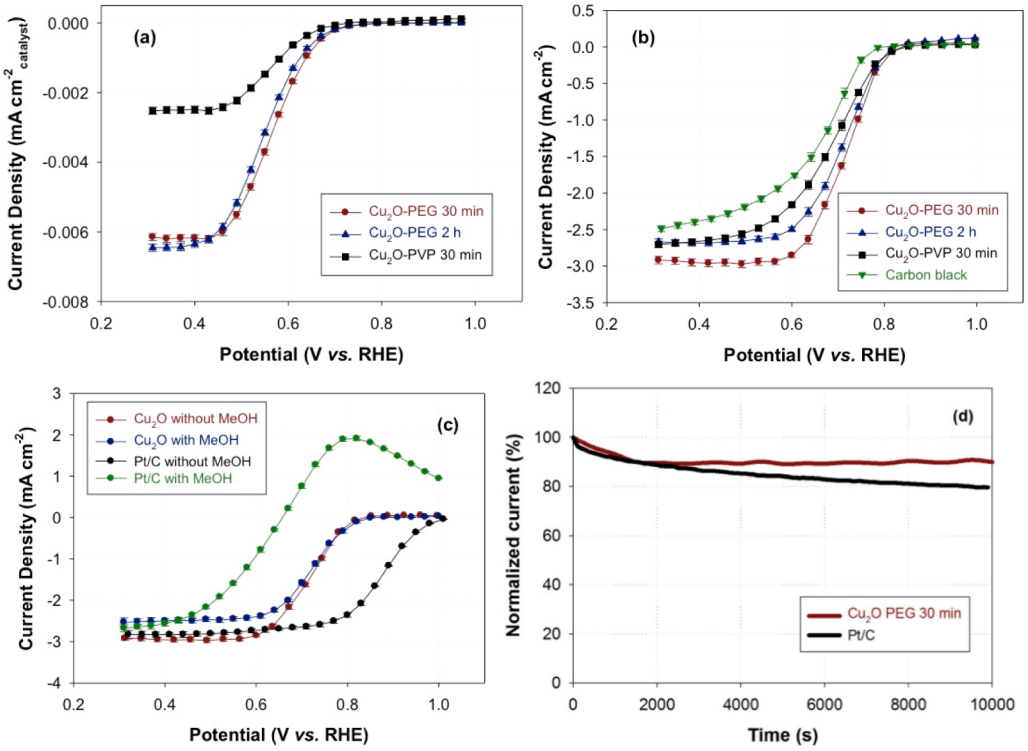

Figure 3. ORR steady-state polarization curves for (a) three pure Cu_2O samples, (b) carbon-supported Cu_2O samples and commercial carbon black in an O_2-saturated 0.1 M KOH electrolyte, and (c) Cu_2O-PEG 30 min and commercial Pt/C catalysts in an O_2-saturated 0.1 M KOH in the presence/absence of 1 M methanol at room temperature, rotating speed: 900 rpm. (d) Chronoamperometric responses of Cu_2O-PEG 30 min and Pt/C electrodes (normalized current vs time) kept at 0.65 V in an O_2-saturated 0.1 M KOH.

samples studied in this work can be calculated according to the gravimetric double layer capacitance C (F/g) at a given scan rate (v) according to eq 6[47]

$$C = I/vm \tag{6}$$

where I is the current and m is the electrode mass. The specific S_a value can be estimated from the gravimetric capacitance C of the Cu_2O samples by the eq 7

$$S_a = C/C_{GC} \tag{7}$$

where C_{GC} is the double layer capacitance (F/m^2) of the glassy carbon electrode surface, for which the typical value of 0.2 F/m^2 was used. The calculated S_a for three Cu_2O samples are 23.6 m^2/g (Cu_2O-PEG 30 min), 21.6 m^2/g (Cu_2O-PEG 2 h), and 37.4 m^2/g (Cu_2O-PVP 30 min), respectively. These values are used later to normalize the current density in ORR plots to evaluate the specific activity of Cu_2O samples. ORR steady-state polarization plots for these Cu_2O nanocrystals are compared in Figure 3a. Similar onset potentials (~0.72 V vs RHE) of ORR were measured with these three Cu_2O nanoparticles, indicative of the same nature of active site. However, the ORR activity in the kinetic range is greatly morphology- and/or structure-dependent. Compared to porous Cu_2O nanoparticles (with both {111} and {100} crystal planes), truncated Cu_2O nanocubes collected at a reaction time of 2 h (also with both {111} and {100} crystal planes) exhibit superior ORR activity, with a more positive half-wave potential ($E_{1/2}$) at 0.55 V and an improved current density in mass transport-controlled potential regions. It is somehow disappointing that the presence of porous structures in PVP-assisted Cu_2O with increased surface area fails to show improved electrocatalytic activity. However, this might be again proving that robust surface coverage of Cu_2O by PVP will limit the access by O_2 during Cu_2O synthesis and electrocatalytic activity (ORR) measurement. In order to thoroughly remove PVP from the Cu_2O surface, the PVP-assisted Cu_2O sample was subjected to an annealing process at 400 °C in a N_2 atmosphere for 1 h.[48] However, the ORR activity measured with the Cu_2O after heat treatment is greatly reduced as shown in Figure S5. This is most likely due to the significant agglomeration of porous Cu_2O particles during the annealing process, as evidenced by the TEM images (Figure S6). As for the Cu_2O nanocubes prepared in a relative short time (dominated by {100} crystal planes), its ORR $E_{1/2}$ is further shifted from 0.55 to 0.57 V. These results indicate an enhanced kinetic rate for the ORR can be achieved on Cu_2O nanocubes as compared to porous nanoparticles. Thus, ORR for Cu_2O nanoparticles is structure-dependent and the reaction activity on Cu_2O {100} plane is higher than that on {111} plane. The exposed crystal facets of the catalysts were closely correlated with their catalytic activity. For instance, Tian et al.[1] reported Pt tetrahexahedra with exposed high-index planes (e.g., {730}, {210}, and {520} facets) exhibited higher activity for ethanol oxidation compared to a commercially available Pt/C catalyst dominant with low-index planes such as {111} and {100}. In this work, the electrochemical measurements demonstrate the ORR activity on Cu_2O {100} plane is higher than that on {111} plane. That indicates the orientation of the steps and terraces of {100} plane is more favorable for the ORR than that of {111} plane, providing the optimal binding energy between Cu_2O and the adsorbed reaction intermediates in the ORR. It can be also attributed to the probably more active sites located at edges and/or corners of the Cu_2O nanocubes with dominant {100} crystal facets exposed. As for the working mechanism of Cu_2O as an ORR catalyst, we think in charge

dx.doi.org/10.1021/jp403655y | J. Phys. Chem. C 2013, 117, 13872−13878

control potential ranges, along with the first-order dependence on O_2 partial pressure, there is a rate-limiting first electron transferring to adsorbed O_2 to form superoxide on Cu_2O (eq 8), possibly involving a concurrent reaction with water (eq 9).[49]

$$Cu_2O - O_2 + e^- \rightarrow Cu_2O - O_2^- \quad (8)$$

$$Cu_2O - O_2 + H_2O + e^- \rightarrow Cu_2O - HO_2 + OH^- \quad (9)$$

However, it is noteworthy that the ORR limiting currents measured with three Cu_2O samples are significantly lower than the theoretical value of ~3.0 mA cm^{-2}, assuming four electrons are involved in ORR at a rotating speed of 900 rpm, which is estimated based on the boundary-layer diffusion-limiting current equation derived from a modified Koutecky–Levich equation (eq 10)[50]

$$j_d = 0.62nAFD_0^{2/3}C_o\nu^{-1/6}\omega^{1/2} \quad (10)$$

where n is the number of electrons involved in ORR, F is the Faraday constant (96485 C/mol), D_0 is the diffusion coefficient of O_2 (1.9×10^{-5} cm^2/s), ω is the electrode rotation rate in units of rpm, ν is the kinematic viscosity of water (0.01 cm^2/s), and C_0 is the concentration of O_2 in diluted aqueous solution (1.1×10^{-6} mol/cm^3). We believe the significant suppression of limiting currents is most likely due to the polymer residuals and/or insufficient conductivity on the Cu_2O surface. These will prevent the accessibility of active sites by O_2 in the mass transfer potential range, resulting in a reduced limiting current density as observed in Figure 3a. In order to mitigate such influences, Cu_2O is further forced to impregnate a carbon black (Ketjenblack EC-300J), and the ORR polarization plots of the resulting carbon-dispersed Cu_2O samples are displayed in Figure 3b. Expected ORR limiting currents are observed with all three carbon-Cu_2O samples, revealing the positive effect of carbon in relieving the performance penalty induced by the polymer residuals and/or insufficient conductivity. Importantly, the ORR activity measured with three carbon-Cu_2O samples shows the same trend as pure Cu_2O without adding carbon black (Figure 3a). The PEG-assisted Cu_2O nanocubes dominated by {100} crystal planes also shows the most positive $E_{1/2}$ (ca. 0.72 V). These results suggest that the intrinsic activity of different Cu_2O samples in kinetic range is independent of the introduction of carbon support. In the meantime, all three carbon-supported Cu_2O reveal better ORR activity than carbon black in terms of ORR onset potential and half-wave potential, indicating the inherent high ORR activity of Cu_2O and a possible synergistic effect between Cu_2O and carbon black.

The ability to catalyze ORR in the presence of methanol is highly required for the catalysts used in the direct methanol fuel cells (DMFCs) due to the severe methanol crossover from anode to cathode. The methanol tolerance of the catalysts for ORR was evaluated in O_2-saturated 0.1 M KOH in the presence of 1 M methanol. As shown in Figure 3c, the commercial Pt/C has a significant current peak at +0.8 V in the presence of methanol, caused by the competition between methanol oxidation and oxygen reduction. Apparently, ORR current on Pt/C was markedly overwhelmed by the methanol oxidation current, indicating a poor methanol tolerance of Pt/C. However, the ORR activity of the Cu_2O catalyst was much less affected by methanol and the ORR activity is superior to that on Pt/C catalyst, suggesting the potential use of this catalyst in direct methanol fuel cells. Durability tests demonstrate that the Cu_2O electrode is exceptionally stable, with a slight decrease after the first 2000 s (Figure 3d) and the resulting current after 10 000 s remains ~91% of the initial value. In contrast, the degradation of Pt/C catalyst is quite significant due to Ostwald ripening, particle aggregation, and carbon corrosion,[51] with a sustained current loss (larger than 20%) after the durability test.

The four-electron selectivity during the ORR was investigated using electron transfer number (n) and peroxide yield. The results for three different Cu_2O samples are displayed in Figure 4 and are in good agreement with the overall activity.

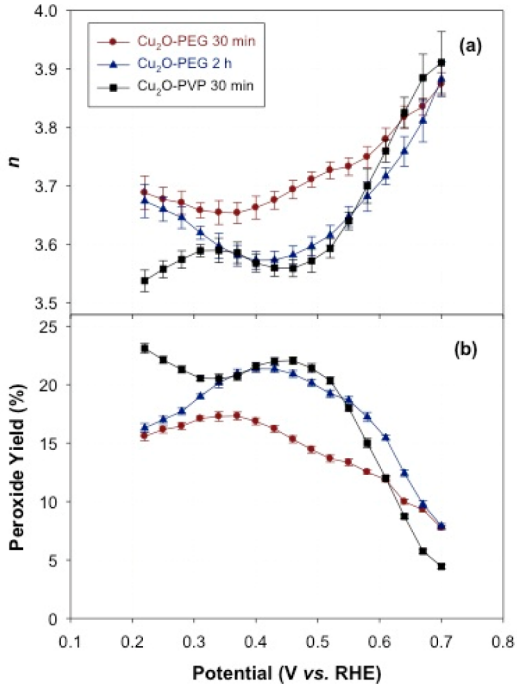

Figure 4. Electron transfer number (n) (a) and peroxide yield (b) of three Cu_2O samples at various potentials based on the corresponding RRDE data.

Cu_2O nanocubes exhibit the highest four-electron selectivity for ORR with electron transfer number of n = 3.7 and peroxide yield of 15%. Therefore, in comparison with {111} plane, {100} plane of Cu_2O nanocrystals is more efficiently catalyzing the reduction of O_2 to OH^- ions, mainly through a direct four-electron or a two + two route. Though truncated Cu_2O nanocubes and nanoporous Cu_2O show slightly reduced ORR selectivity, they still can be comparable NMPCs for ORR.

Tafel slope (b) was calculated from kinetic current density (j_k) to evaluate the ORR mechanism on these Cu_2O nanoparticle samples. According to the Koutecky–Levich equation (eq 11), j_k is derived from the steady-state (j) and diffusion-limiting current density (j_d).

$$j_k = jj_d/(j_d - j) \quad (11)$$

Figure 5 shows the representative Tafel plots of ORR on three different Cu_2O samples. The Tafel slopes calculated for three Cu_2O nanoparticles are nearly identical around −87 mV dec^{-1}, suggesting the similar reaction mechanism with the same rate-determining step (RDS). Theoretically, a Tafel slope of −120 mV dec^{-1} is considered as an RDS that is associated with the first-electron transfer, while a Tafel slope of −59 mV dec^{-1} can be explained by a migration of adsorbed oxygen intermediates on catalysts with a Temkin isotherm as the RDS.[52] Here, the

dx.doi.org/10.1021/jp403655y | J. Phys. Chem. C 2013, 117, 13872−13878

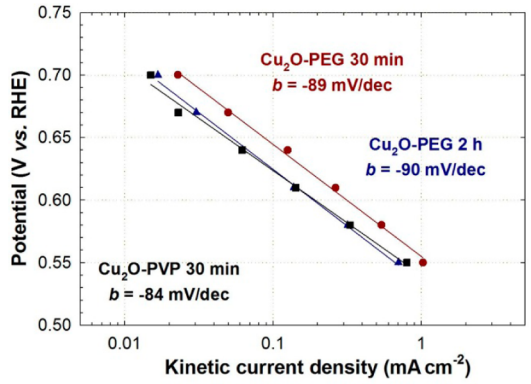

Figure 5. Tafel plots for the ORR on PEG-assisted and PVP-assisted Cu_2O nanocrystals.

measured Tafel slopes between −120 and −59 mV dec^{-1} indicate that oxygen reduction on Cu_2O nanocrystals is controlled simultaneously by charge transfer and intermediate migration. Different catalytic activity observed for these Cu_2O nanoparticles may be related to the rates of charge transfer or intermediate migration, as a function of different crystal planes and other possible structure features (size or morphology). Relevant density function theory (DFT) calculation is ongoing to identify and evaluate the involved charge and mass transfer properties for Cu_2O nanocrystals.

IV. CONCLUSIONS

In summary, a series of Cu_2O nanoparticles with different structure and morphology ranging from nanocubes, sphere-like truncated nanocubes, to nanoporous morphology have been prepared via a solution chemistry route. Each kind of Cu_2O nanoparticles is dominated by certain crystal plane(s) and morphology. Nanocubes are {100} single crystals, while both {111} and {100} crystal planes are present in the truncated sphere-like and nanoporous Cu_2O. The structure-dependent electro-catalytic properties of Cu_2O nanocrystals toward ORR have been determined in alkaline media. Three Cu_2O samples show the same onset potential, suggesting the identical nature of active site. However, the electrocatalytic activity at kinetic range varies with different Cu_2O crystal planes, where {100} is more active than {111}. Using PVP as capping agent leads to nanoporous Cu_2O and better surface coverage that prevents further oxidation by oxygen; however, it also limits the access for oxygen reduction hence a smaller current density. Cu_2O nanocubes with dominant {100} crystal planes show highest activity and four-electron selectivity for ORR, compared to others. Evaluation of the ORR kinetic character by Tafel slope indicates that oxygen reduction on Cu_2O nanocrystals is controlled by charge transfer and intermediate migration. The electron and intermediate may transfer faster on {100} than on {111} planes. Moreover, the Cu_2O nanocrystals show better methanol tolerance and durability for ORR than the commercial Pt/C materials. The fundamental morphology- and structure-dependent electro-catalytic study will provide a general rule for rational design of Cu_2O-based catalyst with maximum activity.

■ ASSOCIATED CONTENT

Supporting Information

Figure S1−S6. This material is available free of charge via the Internet at http://pubs.acs.org.

■ AUTHOR INFORMATION

Corresponding Author

*E-mail: pxu@hit.edu.cn (P.X.); wugang@lanl.gov (G.W.); hwang@lanl.gov (H.L.W.).

Notes

The authors declare no competing financial interest.

■ ACKNOWLEDGMENTS

P.X. thanks the support from the China Postdoctor Fund, NSFC (No. 21203045, 21101041, 21003029, 21071037, and 91122002), Fundamental Research Funds for the Central Universities (Grant Nos. HIT. NSRIF. 2010065 and 2011017, and HIT.BRETIII. 201223), and Director's Postdoctoral Fellow from LANL. H.L.W. acknowledges the financial support from the Laboratory Directed Research and Development (LDRD) fund under the auspices of DOE. This work is partially supported by Basic Energy Science (BES), Biomaterials program, Materials Sciences and Engineering Division.

■ REFERENCES

(1) Tian, N.; Zhou, Z. Y.; Sun, S. G.; Ding, Y.; Wang, Z. L. Synthesis of Tetrahexahedral Platinum Nanocrystals with High-Index Facets and High Electro-oxidation Activity. *Science* **2007**, *316*, 732−735.

(2) Lim, B.; Jiang, M. J.; Camargo, P. H. C.; Cho, E. C.; Tao, J.; Lu, X. M.; Zhu, Y. M.; Xia, Y. N. Pd-Pt Bimetallic Nanodendrites with High Activity for Oxygen Reduction. *Science* **2009**, *324*, 1302−1305.

(3) Debe, M. K. Electrocatalyst Approaches and Challenges for Automotive Fuel Cells. *Nature* **2012**, *486*, 43−51.

(4) Lee, J. S.; Kim, S. T.; Cao, R.; Choi, N. S.; Liu, M.; Lee, K. T.; Cho, J. Metal-Air Batteries with High Energy Density: Li-Air versus Zn-Air. *Adv. Energy. Mater.* **2011**, *1*, 34−50.

(5) Lee, H.; Habas, S. E.; Kweskin, S.; Butcher, D.; Somorjai, G. A.; Yang, P. D. Morphological Control of Catalytically Active Platinum Nanocrystals. *Angew. Chem. Int. Ed.* **2006**, *45*, 7824−7828.

(6) Huang, X. Q.; Li, Y. J.; Li, Y. J.; Zhou, H. L.; Duan, X. F.; Huang, Y. Synthesis of PtPd Bimetal Nanocrystals with Controllable Shape, Composition, and Their Tunable Catalytic Properties. *Nano Lett.* **2012**, *12*, 4265−4270.

(7) Wu, G.; More, K. L.; Johnston, C. M.; Zelenay, P. High-Performance Electrocatalysts for Oxygen Reduction Derived from Polyaniline, Iron, and Cobalt. *Science* **2011**, *332*, 443−447.

(8) Chen, Z. W.; Higgins, D.; Yu, A. P.; Zhang, L.; Zhang, J. J. A Review on Non-Precious Metal Electrocatalysts for PEM Fuel Cells. *Energ. Environ. Sci.* **2011**, *4*, 3167−3192.

(9) Liang, Y. Y.; Li, Y. G.; Wang, H. L.; Zhou, J. G.; Wang, J.; Regier, T.; Dai, H. J. Co_3O_4 Nanocrystals on Graphene as a Synergistic Catalyst for Oxygen Reduction Reaction. *Nat. Mater.* **2011**, *10*, 780−786.

(10) Debart, A.; Paterson, A. J.; Bao, J.; Bruce, P. G. Alpha-MnO_2 Nanowires: A Catalyst for the O_2 Electrode in Rechargeable Lithium Batteries. *Angew. Chem. Int. Edit* **2008**, *47*, 4521−4524.

(11) Wu, G.; Nelson, M. A.; Mack, N. H.; Ma, S. G.; Sekhar, P.; Garzon, F. H.; Zelenay, P. Titanium Dioxide-Supported Non-Precious Metal Oxygen Reduction Electrocatalyst. *Chem. Commun.* **2010**, *46*, 7489−7491.

(12) Sasaki, K.; Zhang, L.; Adzic, R. R. Niobium Oxide-Supported Platinum Ultra-Low Amount Electrocatalysts for Oxygen Reduction. *Phys. Chem. Chem. Phys.* **2008**, *10*, 159−167.

(13) Imai, H.; Matsumoto, M.; Miyazaki, T.; Fujieda, S.; Ishihara, A.; Tamura, M.; Ota, K. Structural Defects Working as Active Oxygen-Reduction Sites in Partially Oxidized Ta-Carbonitride Core-Shell Particles Probed by Using Surface-Sensitive Conversion-Electron-Yield X-ray Absorption Spectroscopy. *Appl. Phys. Lett.* **2010**, *96*, 191905.

(14) Zhou, Y. X.; Yao, H. B.; Wang, Y.; Liu, H. L.; Gao, M. R.; Shen, P. K.; Yu, S. H. Hierarchical Hollow Co_9S_8 Microspheres:

Solvothermal Synthesis, Magnetic, Electrochemical, and Electrocatalytic Properties. *Chem.—Eur. J.* **2010**, *16*, 12000−12007.
(15) Liu, Y.; Mustain, W. E. Structural and Electrochemical Studies of Pt Clusters Supported on High-Surface-Area Tungsten Carbide for Oxygen Reduction. *ACS Catal.* **2011**, *1*, 212−220.
(16) Chen, J.; Takanabe, K.; Ohnishi, R.; Lu, D. L.; Okada, S.; Hatasawa, H.; Morioka, H.; Antonietti, M.; Kubota, J.; Domen, K. Nano-Sized TiN on Carbon Black as an Efficient Electrocatalyst for the Oxygen Reduction Reaction Prepared Using an mpg-C_3N_4 Template. *Chem. Commun.* **2010**, *46*, 7492−7494.
(17) Briskman, R. N. A Study of Electrodeposited Cuprous-Oxide Photovoltaic Cells. *Sol. Energ. Mater. Sol. C* **1992**, *27*, 361−368.
(18) McShane, C. M.; Choi, K. S. Photocurrent Enhancement of n-Type Cu_2O Electrodes Achieved by Controlling Dendritic Branching Growth. *J. Am. Chem. Soc.* **2009**, *131*, 2561−2569.
(19) de Jongh, P. E.; Vanmaekelbergh, D.; Kelly, J. J. Cu_2O: A Catalyst for the Photochemical Decomposition of Water? *Chem. Commun.* **1999**, 1069−1070.
(20) Hara, M.; Kondo, T.; Komoda, M.; Ikeda, S.; Shinohara, K.; Tanaka, A.; Kondo, J. N.; Domen, K. Cu_2O as a Photocatalyst for Overall Water Splitting under Visible Light Irradiation. *Chem. Commun.* **1998**, 357−358.
(21) Paracchino, A.; Laporte, V.; Sivula, K.; Gratzel, M.; Thimsen, E. Highly Active Oxide Photocathode for Photoelectrochemical Water Reduction. *Nat. Mater.* **2011**, *10*, 456−461.
(22) Sun, S. D.; Song, X. P.; Sun, Y. X.; Deng, D. C.; Yang, Z. M. The Crystal-Facet-Dependent Effect of Polyhedral Cu_2O Microcrystals on Photocatalytic Activity. *Catal. Sci. Technol.* **2012**, *2*, 925−930.
(23) Qiu, C.; Zhang, L.; Wang, H.; Jiang, C. Y. Surface-Enhanced Raman Scattering on Hierarchical Porous Cuprous Oxide Nanostructures in Nanoshell and Thin-Film Geometries. *J. Phys. Chem. Lett.* **2012**, *3*, 651−657.
(24) Park, J. C.; Kim, J.; Kwon, H.; Song, H. Gram-Scale Synthesis of Cu_2O Nanocubes and Subsequent Oxidation to CuO Hollow Nanostructures for Lithium-Ion Battery Anode Materials. *Adv. Mater.* **2009**, *21*, 803−807.
(25) Jang, H. S.; Kim, S. J.; Choi, K. S. Construction of Cuprous Oxide Electrodes Composed of 2D Single-Crystalline Dendritic Nanosheets. *Small* **2010**, *6*, 2183−2190.
(26) Wang, W. Z.; Wang, G. H.; Wang, X. S.; Zhan, Y. J.; Liu, Y. K.; Zheng, C. L. Synthesis and Characterization of Cu_2O Nanowires by a Novel Reduction Route. *Adv. Mater.* **2002**, *14*, 67−69.
(27) Gou, L. F.; Murphy, C. J. Solution-Phase Synthesis of Cu_2O Nanocubes. *Nano Lett.* **2003**, *3*, 231−234.
(28) Kuo, C. H.; Chen, C. H.; Huang, M. H. Seed-Mediated Synthesis of Monodispersed Cu_2O Nanocubes with Five Different Size Ranges from 40 to 420 nm. *Adv. Funct. Mater.* **2007**, *17*, 3773−3780.
(29) Li, X. D.; Gao, H. S.; Murphy, C. J.; Gou, L. F. Nanoindentation of Cu_2O Nanocubes. *Nano Lett.* **2004**, *4*, 1903−1907.
(30) Gou, L. F.; Murphy, C. J. Controlling the Size of Cu_2O Nanocubes from 200 to 25 nm. *J. Mater. Chem.* **2004**, *14*, 735−738.
(31) Zhou, W. W.; Yan, B.; Cheng, C. W.; Cong, C. X.; Hu, H. L.; Fan, H. J.; Yu, T. Facile Synthesis and Shape Evolution of Highly Symmetric 26-Facet Polyhedral Microcrystals of Cu_2O. *CrystEngComm* **2009**, *11*, 2291−2296.
(32) Leng, M.; Liu, M. Z.; Zhang, Y. B.; Wang, Z. Q.; Yu, C.; Yang, X. G.; Zhang, H. J.; Wang, C. Polyhedral 50-Facet Cu_2O Microcrystals Partially Enclosed by {311} High-Index Planes: Synthesis and Enhanced Catalytic CO Oxidation Activity. *J. Am. Chem. Soc.* **2010**, *132*, 17084−17087.
(33) Sun, S. D.; Zhou, F. Y.; Wang, L. Q.; Song, X. P.; Yang, Z. M. Template-Free Synthesis of Well-Defined Truncated Edge Polyhedral Cu_2O Architectures. *Cryst. Growth. Des.* **2010**, *10*, 541−547.
(34) Lu, C. H.; Qi, L. M.; Yang, J. H.; Wang, X. Y.; Zhang, D. Y.; Xie, J. L.; Ma, J. M. One-Pot Synthesis of Octahedral Cu_2O Nanocages via a Catalytic Solution Route. *Adv. Mater.* **2005**, *17*, 2562−2567.
(35) Siegfried, M. J.; Choi, K. S. Directing the Architecture of Cuprous Oxide Crystals during Electrochemical Growth. *Angew. Chem., Int. Ed.* **2005**, *44*, 3218−3223.
(36) Zhang, L.; Wang, H. Cuprous Oxide Nanoshells with Geometrically Tunable Optical Properties. *ACS Nano* **2011**, *5*, 3257−3267.
(37) Zhang, H. G.; Zhu, Q. S.; Zhang, Y.; Wang, Y.; Zhao, L.; Yu, B. One-Pot Synthesis and Hierarchical Assembly of Hollow Cu_2O Microspheres with Nanocrystals-Composed Porous Multishell and Their Gas-Sensing Properties. *Adv. Funct. Mater.* **2007**, *17*, 2766−2771.
(38) Yang, M.; Zhu, J. J. Spherical Hollow Assembly Composed of Cu_2O Nanoparticles. *J. Cryst. Growth.* **2003**, *256*, 134−138.
(39) Zhang, H. R.; Yu, H. C.; Shen, C. M.; Yang, H. X.; Li, J. Q. TEM Study on Hollow and Porous Cu_2O Nanoparticles Prepared from Solution Phase. *Chin. Phys.* **2006**, *15*, 1290−1295.
(40) Wang, W. Z.; Zhang, P. C.; Peng, L.; Xie, W. J.; Zhang, G. L.; Tu, Y.; Mai, W. J. Template-Free Room Temperature Solution Phase Synthesis of Cu_2O Hollow Spheres. *CrystEngComm* **2010**, *12*, 700−701.
(41) Yan, X. Y.; Tong, X. L.; Zhang, Y. F.; Han, X. D.; Wang, Y. Y.; Jin, G. Q.; Qin, Y.; Guo, X. Y. Cuprous Oxide Nanoparticles Dispersed on Reduced Graphene Oxide as an Efficient Electrocatalyst for Oxygen Reduction Reaction. *Chem. Commun.* **2012**, *48*, 1892−1894.
(42) Zhang, Y.; Deng, B.; Zhang, T. R.; Gao, D. M.; Xu, A. W. Shape Effects of Cu_2O Polyhedral Microcrystals on Photocatalytic Activity. *J. Phys. Chem. C* **2010**, *114*, 5073−5079.
(43) Siegfried, M. J.; Choi, K. S. Elucidating the Effect of Additives on the Growth and Stability of Cu_2O Surfaces via Shape Transformation of Pre-Grown Crystals. *J. Am. Chem. Soc.* **2006**, *128*, 10356−10357.
(44) Wang, D. B.; Mo, M. S.; Yu, D. B.; Xu, L. Q.; Li, F. Q.; Qian, Y. T. Large-Scale Growth and Shape Evolution of Cu_2O Cubes. *Cryst. Growth Des.* **2003**, *3*, 717−720.
(45) Zhang, J. T.; Liu, J. F.; Peng, Q.; Wang, X.; Li, Y. D. Nearly Monodisperse Cu_2O and CuO Nanospheres: Preparation and Applications for Sensitive Gas Sensors. *Chem. Mater.* **2006**, *18*, 867−871.
(46) Zhang, L.; Li, H.; Ni, Y. H.; Li, J.; Liao, K. M.; Zhao, G. C. Porous Cuprous Oxide Microcubes for Non-Enzymatic Amperometric Hydrogen Peroxide and Glucose Sensing. *Electrochem. Commun.* **2009**, *11*, 812−815.
(47) Wu, G.; Swaidan, R.; Li, D. Y.; Li, N. Enhanced Methanol Electro-Oxidation Activity of PtRu Catalysts Supported on Heteroatom-Doped Carbon. *Electrochim. Acta* **2008**, *53*, 7622−7629.
(48) Gu, Y. L.; Wu, G.; Hu, X. F.; Chen, D. A.; Hansen, T.; zur Loye, H. C.; Ploehn, H. J. PAMAM-Stabilized Pt-Ru Nanoparticles for Methanol Electro-oxidation. *J. Power Sources* **2010**, *195*, 425−434.
(49) Sepa, D. B.; Vojnovic, M. V.; Damjanovic, A. Kinetics and Mechanism of O_2 Reduction at-Pt in Alkaline-Solutions. *Electrochim. Acta* **1980**, *25*, 1491−1496.
(50) Newman, J. Schmidt Number Correction for Rotating Disk. *J. Phys. Chem.* **1966**, *70*, 1327−1328.
(51) Chen, Z. W.; Waje, M.; Li, W. Z.; Yan, Y. S. Supportless Pt and PtPd Nanotubes as Electrocatalysts for Oxygen-Reduction Reactions. *Angew. Chem., Int. Ed.* **2007**, *46*, 4060−4063.
(52) Coutanceau, C.; Croissant, M. J.; Napporn, T.; Lamy, C. Electrocatalytic Reduction of Dioxygen at Platinum Particles Dispersed in a Polyaniline Film. *Electrochim. Acta* **2000**, *46*, 579−588.